

Supplementary Materials

Wedding Cake Growth Mechanism in One-Dimensional and Two-Dimensional Nanostructure Evolution

Xin Yin,¹ Jian Shi,^{1,2} Xiaobin Niu,^{3,4} Hanchen Huang,³ Xudong Wang^{1*}

1. Department of Materials Science and Engineering, University of Wisconsin-Madison, Madison, Wisconsin 53706, United States
2. Department of Materials Science and Engineering, Rensselaer Polytechnic Institute, Troy, New York 12180, United States
3. Department of Mechanical and Industrial Engineering, Northeastern University, Boston, Massachusetts 02115, United States
4. Institute of Fundamental and Frontier Science, State Key Laboratory of Electronic Thin Film and Integrated Devices, University of Electronic Science and Technology of China, Chengdu 610054, P. R. China

*Corresponding author. E-mail: xudong@engr.wisc.edu

S1. Experiment section

S1.1. Synthesis process

5 g zinc oxide powder was weighed as the precursor and loaded in an alumina boat. The boat was then placed at the center of an alumina tube located inside a single-zone tube furnace. Argon carrier gas with the flow rate of 50 sccm was applied and the pressure inside the tube was kept at 53 Pa. Three polycrystalline alumina substrates (11.4 cm in length and 1 cm in width) were lined together in the tube which covered a broad deposition temperature. The system temperature reached 1273 K during the first 40 minutes and reached 1673 K after another 50 minutes. The precursor completely decomposed and vaporized before the temperature reached 1673 K. Subsequently, the system was cooled down to room temperature naturally under the same argon atmosphere.

S1.2. Precursor temperature versus time during heating, being constant and cooling down processes

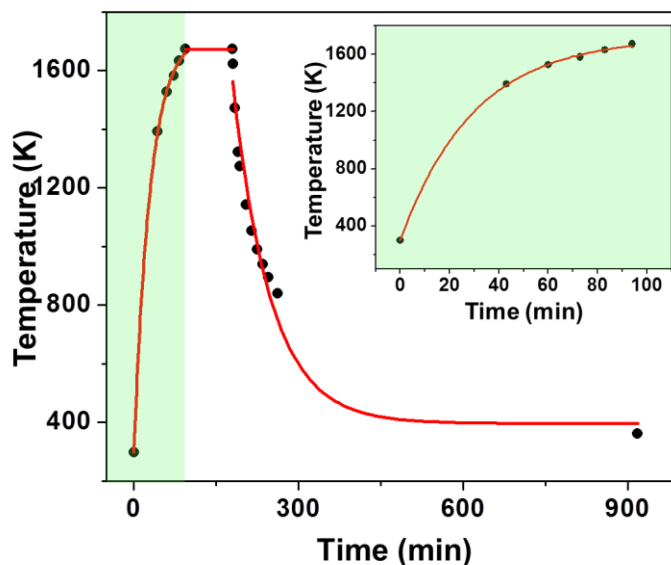


Figure S1. Temperature change during the entire process. The stage for the crystal growth is highlighted in green. The inset is the enlarged curve in the green region.

S1.3. Cross-sectional sample preparation by focused ion beam (FIB)

Zeiss 1540XB CrossBeam Focused Ion Beam FE SEM was used to cut the plate-capped micropillar structure by the flux of gallium ions along the axis of the rod. Because ions flux may

damage the surface feature, a 50-nm-thick layer of carbon and a platinum layer were deposited on the sample for protection of the surface feature.

S1.4. Sample characterization method

Zeiss LEO 1530 Schottky-type field-emission scanning electron microscope was used to study the morphologies of the samples. X-ray diffraction was acquired from Bruker D8 Discovery with Cu $K\alpha$ radiation. FEI TF30 transmission electron microscope operated at 300 kV and C_s -corrected FEI Titan transmission electron microscope operated at 200 kV were used to study the crystal structure of the samples.

S2. Plate-caped micropillars on alumina substrate

The microplate-caped micropillar structure was sparsely distributed on Al_2O_3 substrate. The substrate temperature was around 1670 K.

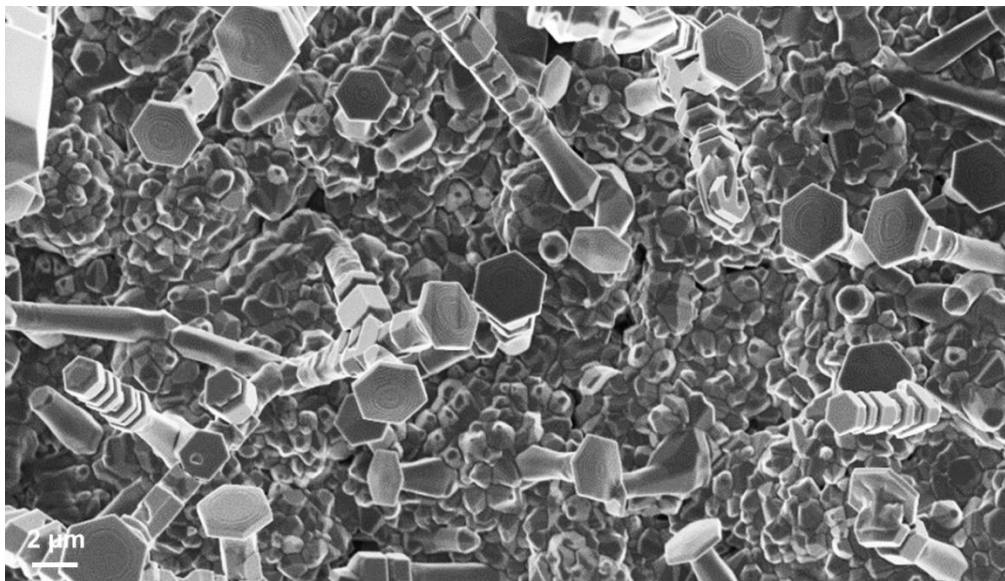


Figure S2. Large scale SEM image of the plate-caped micropillars

S3. XRD analysis

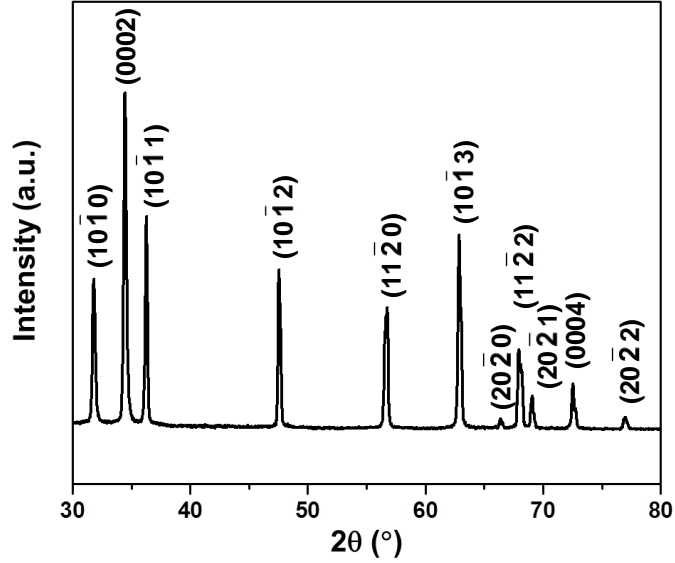


Figure S3. XRD pattern of the ZnO samples confirming the wurtzite crystal structure

S4. Lattice kinetic Monte Carlo simulation of the evolution of suspended microplate at the tip of micropillar

Lattice kinetic Monte Carlo (LKMC) method was performed to simulate the morphology evolution when the SE barrier becomes tangible. In the simulation, both the diffusion barrier and the Ehrlich-Schwoebel (ES) barrier were introduced in order to study ES barrier controlled growth. The growth process was carried out at room temperature instead of 1670 K to keep the outcome structure size under the limit of the simulation power. The deposition on all the other surfaces was neglected except (0001). Adatom horizontal and vertical diffusions on the surfaces were introduced, with a diffusion barrier E_{sd} . Adatom diffusing over a single-layer step with an ES barrier E_{2D} and a multi-layer step with an ES barrier E_{3D} were also applied in the simulation, either downwards or upwards. The jumping frequency is $\nu = \nu_0 e^{-E/kT}$, where the prefactor ν_0 is $5 \times 10^{11} \text{ s}^{-1}$ based on molecular dynamics simulations¹. Since the lack of ZnO ES barrier data, we chose the diffusion barrier energies according to those of Cu^{2, 3}. Thus, we determined the jumping frequency ν , ν_{2D} , and ν_{3D} with the barriers $E_d = 0.10 \text{ eV}$, $E_{2D} = 0.28 \text{ eV}$, and $E_{3D} = 0.70 \text{ eV}$. This simple, generic model should capture the essential physics in the growth we are

interested in. It should be noted that the side wall of the simulated rods are set to be $(11\bar{2}1)$. Due to the nature of the simulation lattice, the lateral size of the output nanorod is gradually reduced as shown in Figure 3B. However, the discussed mechanism for the microplate formation is generally applied and not affected by the side facets orientation.

S5. Supersaturation and Zinc vapor pressure equations

The supersaturation is defined as following ⁴:

$$\sigma = \frac{P}{P_e} - 1 \quad (\text{S1})$$

Zinc vapor pressure is determined by the temperature following the equation ⁵:

$$\log \frac{P}{P_0} = -22.56 \frac{T_0}{T} + 5.233 \quad (\text{S2})$$

where the reference temperature T_0 is 273.15 K and the reference pressure P_0 is 10^5 Pa.

S6. Axial growth rate and lateral growth rate calculation

Table S1. Physical constants (including symbol, value, unit and reference) used for calculating the axial and lateral growth rates.

Quantity	Symbol	value	units	Ref.
Lattice Constant	a	3.25×10^{-10}	m	6
Vibration Frequency	ν	1×10^{13}	s^{-1}	7
Dissociation Heat	$\varphi_{1/2}$	4.70×10^{-19}	J/atom	8
Boltzmann Constant	k	1.38×10^{-23}	J/K	9
Kink Sites Spacing	δ	1.20×10^{-9}	M	7
Specific Edge Energy	η	3.92×10^{-10}	J/m	7
Desorption Energy	E_{des}	2.35×10^{-19}	J/atom	7
Mean Free Path Length	λ_s	4.87×10^{-8}	m	7
Kinetics Barrier	ΔU	3.00×10^{-19}	J/atom	10

In screw dislocation growth model, the characteristic supersaturation (σ_c) is a specific point where the axial growth rate is a parabolic function of the supersaturation when $\sigma < \sigma_c$ and is a linear function of the supersaturation when $\sigma > \sigma_c$. σ_c is expressed as below ⁷:

$$\sigma_c = \frac{19\eta a^2}{2kT\lambda_s} \quad (S3)$$

The mean free path length is obtained from the following equation ⁷:

$$\lambda_s = a \exp\left(\frac{E_{des} - E_{sd}}{2kT}\right) \quad (S4)$$

where E_{sd} is the surface diffusion energy barrier. Because the desorption energy E_{des} is always much greater than the diffusion energy barrier E_{sd} , we can neglect E_{sd} in the exponential term.

S7. Determine the axial to lateral growth rate ratio as a function of supersaturation from the numbers of terraces

S7.1. Relationship between the numbers of terraces and the corresponding growth positions

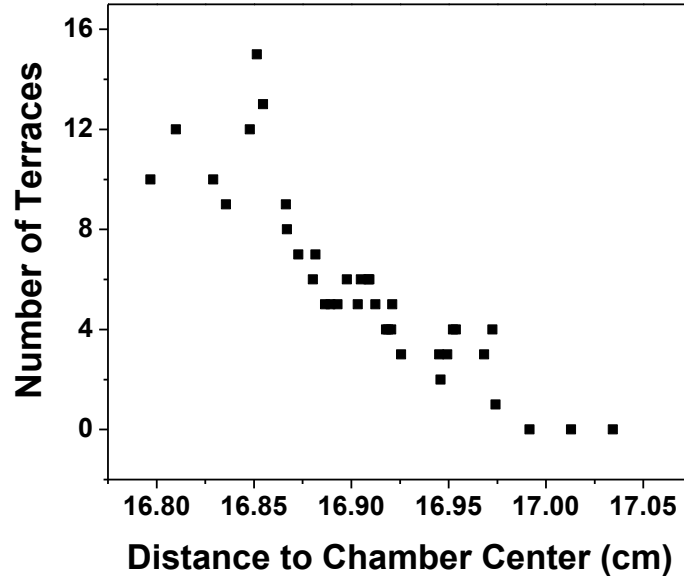


Figure S4. Number of terraces counted on 37 microplate surfaces collected within a 2 mm region where the plate-capped micropillar structures were formed. This region starts at 16.7968 cm from the center of the deposition chamber.

S7.2. Conversion of number of terraces to growth rate ratio

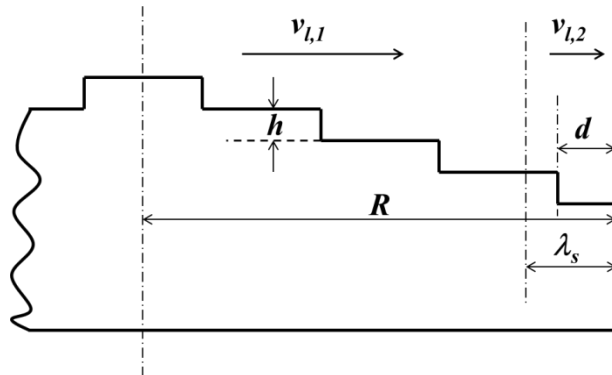


Figure S5. Schematic of the wedding cake growth model. R is the plate radius. λ_s is the mean free path length. d is the distance from the base terrace edge to the plate edge. h is the height of one step. $v_{l,1}$ and $v_{l,2}$ are the lateral growth rates.

Prior to the conversion, the lateral growth process at atomic level needs to be considered in order to clearly illustrate the growth rate. The surface of all plates shows that the terrace outlines become denser near the edge (Figure 3C). This suggests that v_l might not be a constant during the terrace growth. The terraces could initially spread out fast from the center and subsequently slow down when approaching the plate edge. This could be attributed to the narrowing of the effective adatom collection area. Here, we assume all the adatoms adsorbed within λ_s could be incorporated to the ledge front, which determines the maximum effective adatom collection area. At early stage, the width of each terrace is larger than λ_s , therefore the ledge advances with the full velocity as determined by the supersaturation (Eq. 1 in main text). When the ledge front approaches the edge, the effective adatom collection area becomes less than λ_s . Thus, fewer amount of adatoms are incorporated and lower growth velocity is resulted. By rearranging the expression of lateral growth rate for monolayer steps (Eq. 1), the relation is displayed as below:

$$v_{l,mono} = \frac{2\sigma v \exp(-\frac{\phi_{1/2}}{kT})}{1 + \frac{\delta}{a} \exp(\frac{2\Delta U - E_{des}}{2kT})} \lambda_s \quad (S5)$$

For any given plate structure, we assume σ and T are constant, and thus the lateral growth rate is linearly related to λ_s . Therefore, when λ_s decreases, $v_{l,mono}$ decreases. The bunched steps have a lower advance velocity than monolayer steps due to the increased sites for the adatoms. Since the growth of the bunched steps share the same mechanism as the monolayer steps, which is the attachment process of the adatoms, the growth of bunched steps follow the same equation as monolayer steps (displayed in Eq. S5) except an extra coefficient should be added to represent the increased amount of kinks of higher steps. Therefore, the bunched steps also exhibit a linear relation between v_l and λ_s , which will be used to convert the number of terraces to the axial to lateral growth rate ratio.

To determine axial to lateral growth rate ratio, we assume the time spent by the first terrace (the base terrace) to grow from the plate center to the plate edge (t_l) equals to the time to evolve

the rest terraces (t_a). The base terrace expands with a velocity of $v_{l,1}$ and then decreases to $v_{l,2}$ when approaching the edge due to the decrease of effective adatom collection area ($t_l = t_{l,1} + t_{l,2}$). The height from the base terrace to the plate top is nh , where n is the number of the terraces and h is the height of one step. Thus,

$$t_a = \frac{nh}{v_a} = \frac{R - \lambda_s}{v_{l,1}} + t_{l,2} \quad (\text{S6})$$

where R is the plate radius. From the equation of the lateral growth rate (Eq. S5), we can get the expression for $v_{l,1}$:

$$v_{l,1} = A\lambda_s \quad (\text{S7})$$

where the coefficient A is a constant by assuming that σ and T are constant during the growth of a specific microplate:

$$A = \frac{2\alpha\sigma\nu \exp(-\frac{\phi_{1/2}}{kT})}{1 + \frac{\delta}{a} \exp(\frac{2\Delta U - E_{des}}{2kT})}$$

where α ($\alpha < 1$) is a coefficient to present the increased requirement of adatom number due to the multilayer steps.

As for $v_{l,2}$:

$$v_{l,2} = A(\lambda_s - x) \quad (\text{S8})$$

where x is the distance the terrace grows with the velocity $v_{l,2}$. $(\lambda_s - x)$ represents the distance from the terrace edge to the plate edge. This equation expresses the instantaneous velocity at the point $(\lambda_s - x)$ because $v_{l,2}$ varies with the effective collection area. $v_{l,2}$ can be expressed in terms of $v_{l,1}$ as:

$$v_{l,2} = \frac{\lambda_s - x}{\lambda_s} v_{l,1} \quad (\text{S9})$$

Then $t_{l,2}$ can be obtained by integrating from $x = 0$ to $x = (\lambda_s - d)$:

$$t_{l,2} = \int_0^{\lambda_s - d} \frac{dx}{v_{l,2}} = \int_0^{\lambda_s - d} \frac{dx}{\frac{\lambda_s - x}{\lambda_s} v_{l,1}} = \frac{\lambda_s}{v_{l,1}} \ln \frac{\lambda_s}{d} \quad (\text{S10})$$

Insert Eq. S10 into Eq. S6, we get:

$$\frac{nh}{v_a} = \frac{R - \lambda_s}{v_{l,l}} + \frac{\lambda_s}{v_{l,l}} \ln \frac{\lambda_s}{d} \quad (\text{S11})$$

Rearrange Eq. S11 to get the growth rate ratio:

$$\frac{v_a}{v_{l,l}} = \frac{nh}{(R - \lambda_s) + \lambda_s \ln \frac{\lambda_s}{d}} \quad (\text{S12})$$

The values of n , h and d can be obtained by measurement and λ_s can be obtained from Eq. S4, therefore the number of terraces n is converted to the growth rate ratio $v_a/v_{l,l}$.

S7.3. Conversion of plate positions to the supersaturation

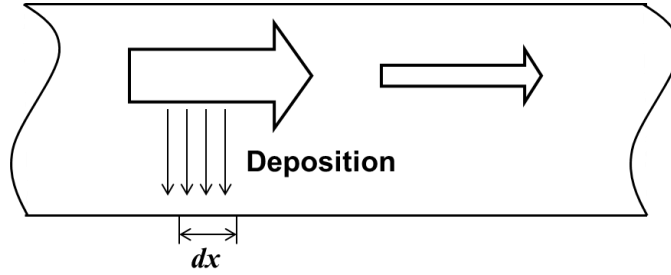


Figure S6. Schematic of the deposition process

Since the deposition region of the plate-caped micropillar structure was only 2 mm, we can assume the temperature is constant in that region (1670 K). Thus the supersaturation is not affected by temperature. Since significant amount of deposition occurred in this region, the zinc vapor concentration decreases due to the consumption of deposition, which is considered as the solo parameter that changes the supersaturation (decreases along the downstream direction).

The local vapor pressure is obtained by subtracting the amount consumed by deposition from the initial amount yielded by the precursor source. According to the previous results¹¹, the deposition of ZnO from the vapor phase undergo two steps, zinc condensation and zinc oxidation. At high temperature (>700 K), the condensation of zinc is the rate-limiting step. Therefore, we use the condensation rate of zinc as the deposition rate. The condensation rate is determined by the sticking coefficient (S) and the incident molecular flux (F) via $R_{con} = F \times S$, where S is estimated to be 0.1¹² and F is obtained from the Hertz-Knudsen equation¹³:

$$F = \frac{P - P_e}{(2\pi mkT)^{1/2}} \quad (\text{S13})$$

where P is the partial pressure of zinc, P_e is the equilibrium partial pressure of zinc at the deposition location, m is the mass of zinc atom, and T is the local temperature (1670 K in this case). Because there was no deposition prior zinc vapor reached the growth region of plate-caped micropillar structure, we can use the total amount yielded by the precursor as the initial partial pressure of zinc to calculate the condensation rate of zinc for the formation of plate-caped micropillar structure.

The unit for zinc condensation rate R_{con} is $mol/(m^2 \cdot s)$. It gives the deposition amount per second per square meter. For an infinitesimal distance dx , the deposition time is dx/r , where r is the flow rate of the carrier gas. The flow rate was obtained from the flowmeter of the CVD system, and then converted to the flow rate in the growth chamber considering the pressure and temperature in the chamber by a rough estimation using $PV = nRT$. The deposition area is the internal surface of the tubular chamber, $\pi \cdot D \cdot dx$, where D is the internal diameter of the furnace tube. The deposition volume is $\pi(D/2)^2 dx$. Thus, the amount of deposition at this infinitesimal area per unit volume (*i.e.* the vapor concentration reduction) is

$$\Delta c = \frac{\pi \cdot D \cdot dx \cdot \frac{dx}{r} \cdot R_{con}}{\pi \cdot \left(\frac{D}{2}\right)^2 \cdot dx} \quad (S14)$$

Eq. S14 is rearranged and simplified as:

$$\Delta c = \frac{4R_{con}}{D \cdot r} \cdot x \quad (S15)$$

where x is the distance from the deposition starting point to the point of interest. The deposition starting point can be measured from the experiment.

Using $P = cRT$ to convert the concentration to pressure, we can combine Eq. S15 and Eq. S1 to get:

$$\sigma = \frac{(c_0 - \frac{4R_{con}}{D \cdot r} \cdot x)RT}{P_e} - 1 \quad (S16)$$

Arranging Eq. S16, we have:

$$\sigma = \frac{c_0 RT - P_e}{P_e} - \frac{4R_{con} \cdot RT}{P_e \cdot D \cdot r} \cdot x \quad (S17)$$

Through this equation, the position of the microplate can be converted to the local supersaturation.

S8. Lateral and axial growth rate ratio in wedding cake growth model

Axial growth rate is determined by the nucleation rate of a new layer on the current top layer. The nucleation of a new layer occurs only when the current top terrace reaches a critical size R_c .¹⁴ Therefore, the axial growth rate can be developed as the axial height change during the time that the growth of the current top terrace takes to the critical size¹⁵. The axial growth rate can be expressed as

$$v_{a,w} = \frac{h}{R_c} v_l \quad (\text{S19})$$

where h is the height of the newly formed terrace, R_c is the critical of the top terrace. It should be noted that the supersaturation has an impact not only on v_l but also on R_c . Therefore, the microplates have different R_c due to the different supersaturation. For each microplates, the axial to lateral growth rate ratio was calculated. Then a linear fitted line was obtained for the relation between growth rate ratio and supersaturation.

S9. NW with terraced tip feature

Nanowires were grown at higher deposition temperature compared to the microplate structure, where the local vapor supersaturation was also higher. Under this condition, the formation of capping plate was suppressed due to the elimination of adatoms diffusing down. Therefore, semi-aligned ZnO nanowires were obtained with high density. All the nanowires are unique in size and are typically 500 nm – 1 μ m in diameter and a few hundred micrometers in length (Fig. S7A). All the nanowires exhibited a concentric terraced tip (Fig. S7B and C), which is similar to those observed from microplates.

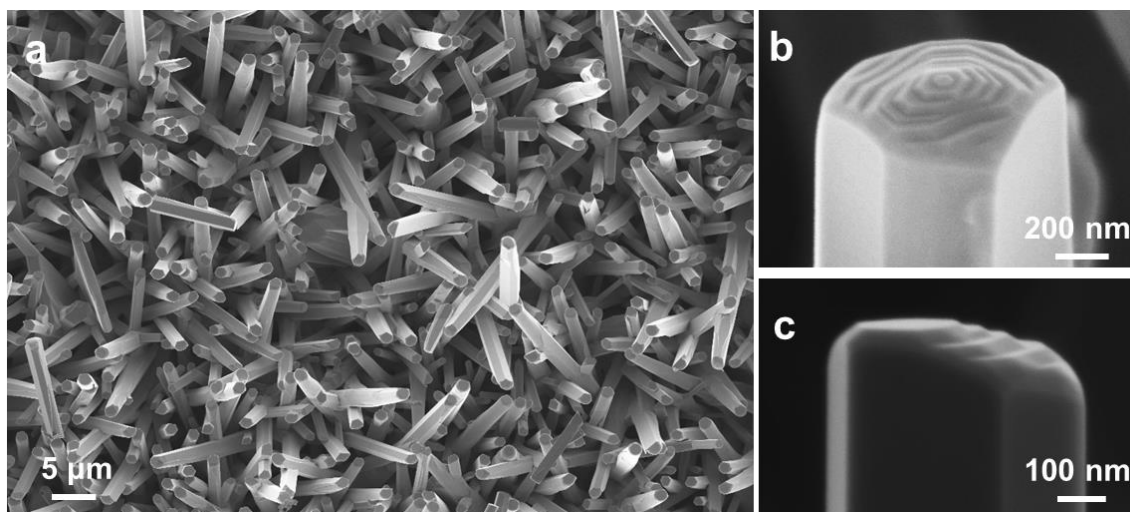


Figure S7. SEM images on Terraced tip feature. **a**, A large scale image on nanowires with terraced tip feature. **(b)** Individual top view and **(c)** side view showing concentric circular mound morphology, reminiscent of a wedding cake.

S10. TEM images on the NW terraced tip feature

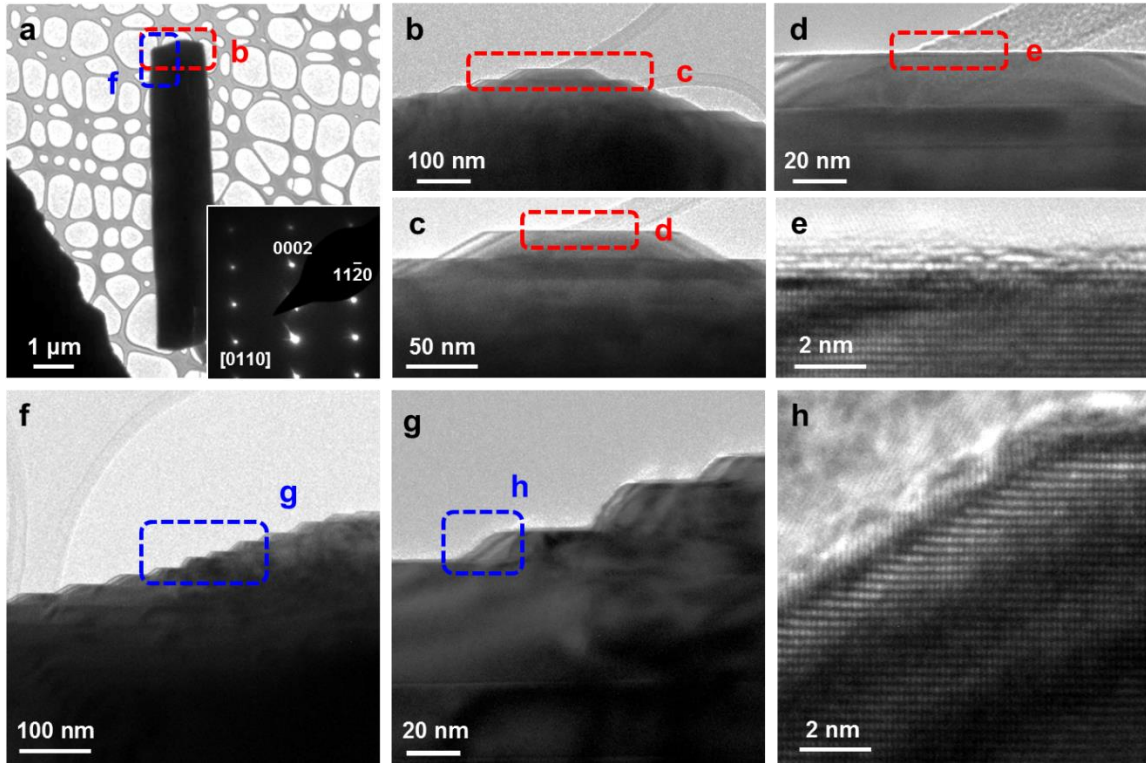


Figure S8. TEM characterization of nanowires with terraced tips. **a**, Low magnification TEM image on an individual nanowire. Inset is the selective area electron diffraction pattern showing the growth direction. **b**, Zoom-in image on terraced tip feature of the nanowire in **a** displaying the wedding cake morphology. **c** and **d** shows the flat and smooth top terrace and no screw dislocation step. **e**, HR-TEM of the top terrace showing the surface is atomic flat. **f** and **g** shows the hillside feature of the wedding cake morphology. **h**, HR-TEM at one step. These features resemble the tip features of the microplates in the plate-capped micropillar structure in Fig. 2.

S11. Number of terraces and coverage change with temperature.

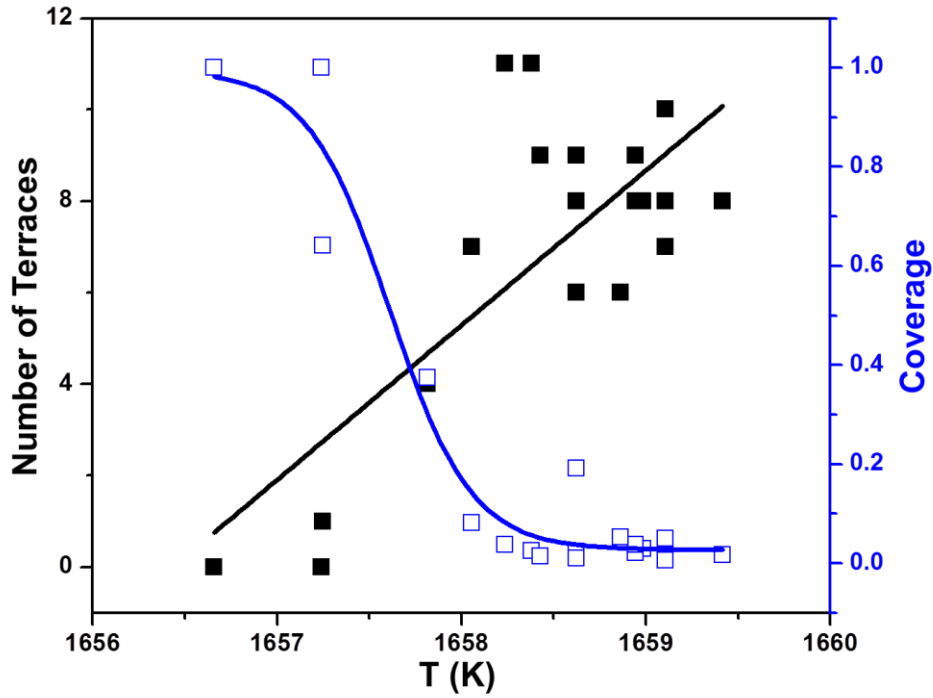


Figure S9. Number of terraces and coverage change with temperature shows the same trend with the microplates in the plate-caped micropillar structure. The coverage is the ratio of the very top layer area to the base layer area on NW tip. It is represented by blue squares and fitted blue line. Black squares and fitted black line represent number of terraces. From the diagram, when temperature decreases, the number of terraces decreases and the coverage approaches to one.

S12. Number of terraces and coverage change with O₂ partial pressure

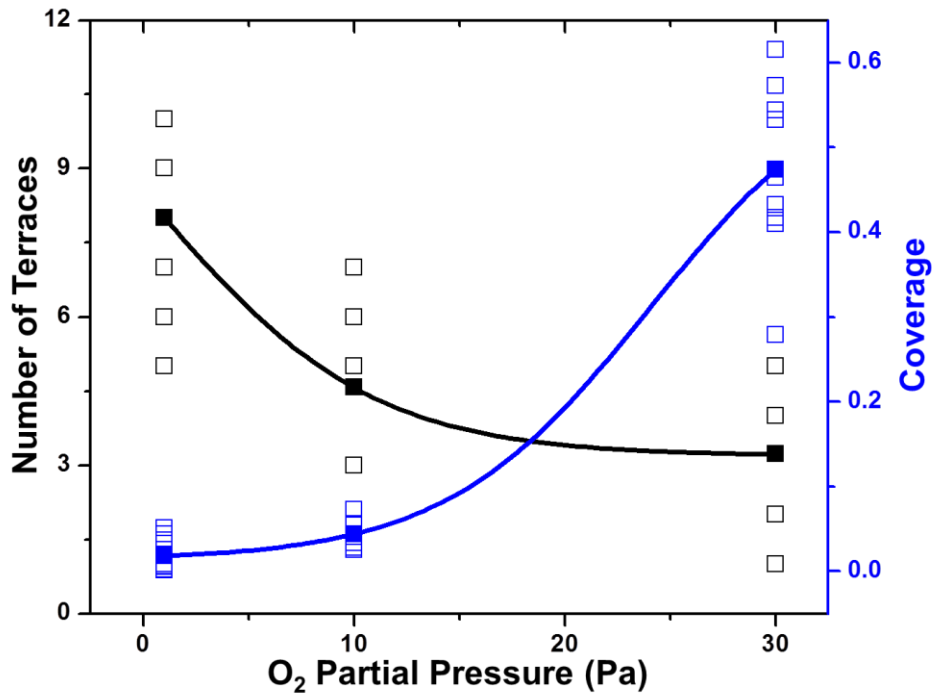


Figure S10. Number of terraces and coverage change with O₂ partial pressure shows the same trend as with temperature. Blue squares represent the coverage. Blue line is the fitted curve based on blue squares. Black squares represent the number of terraces. Black line is the fitted curve based on black squares. Solid squares for both number of terraces and coverage represent the average value at each O₂ partial pressure.

S13. Nanowires with a narrow and long tapered tip

Nanowires with a narrow and long tapered tip were obtained at high supersaturation condition achieved through a sudden reduction of deposition temperature, where the axial growth rate $v_{a,w}$ is much larger than lateral growth rate v_l . As a result, the structures are featured with a much longer tapered tip, compared to the tip in Figure S7.

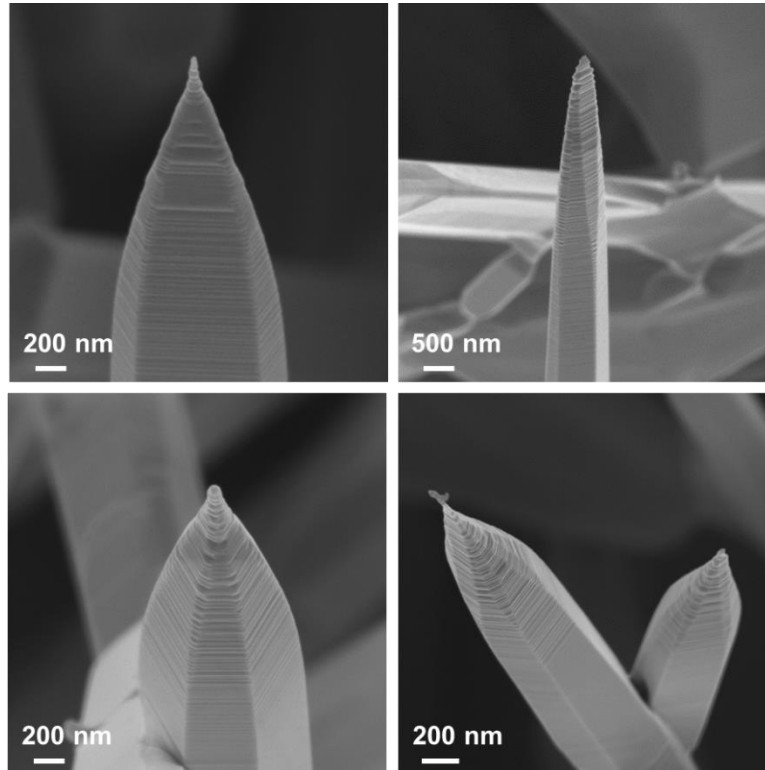


Figure S11. SEM images on nanowires morphology when the axial growth rate $v_{a,w}$ exceeds the growth rate v_l .

S14. SEM image capturing the nucleation of a new layer on the top terrace.

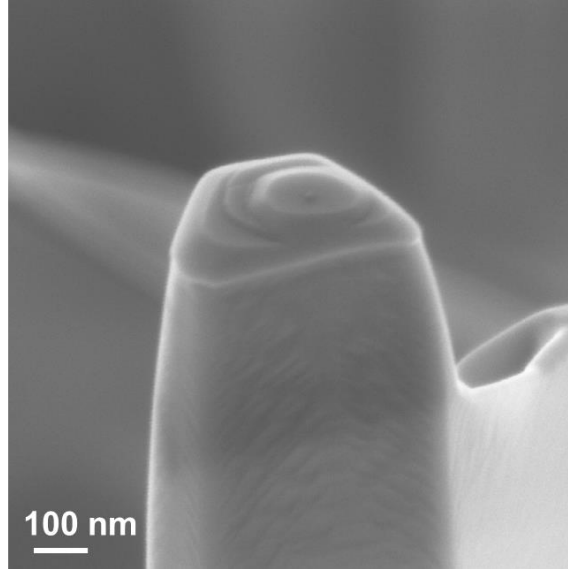


Figure S12. SEM image on the nucleation of a new layer on the top terrace, revealing the growth process of wedding cake growth model.

REFERENCES

1. Kallinteris, G. C.; Evangelakis, G. A.; Papanicolaou, N. I. *Surf. Sci.* **1996**, 369, (1-3), 185-198.
2. Xiang, S. K.; Huang, H. *Appl. Phys. Lett.* **2008**, 92, (10), 101923.
3. Ding, Y.; Wang, X. D.; Wang, Z. L. *Chem. Phys. Lett.* **2004**, 398, (1-3), 32-36.
4. Burton, W. K.; Cabrera, N.; Frank, C. *Philos. Tr. R. Soc. S.-A* **1951**, 243, (866), 299-358.
5. Dorsman, R.; Kleijn, C. R.; Velthuis, J. F. M.; Zijp, J. P.; van Mol, A. M. B. *J. Vac. Sci. Technol. A* **2007**, 25, (3), 474-479.
6. Wang, Z. L. *J. Phys. Condens. Matter* **2004**, 16, (25), R829-R858.
7. Markov, I. V.
8. Yang, Y.; Scholz, R.; Berger, A.; Kim, D. S.; Knez, M.; Hesse, D.; Goesele, U.; Zacharias, M. *Small* **2008**, 4, (12), 2112-2117.
9. Hummel, R. E., *Electronic Properties of Materials, Fourth Edition*. 2011; p 1-488.
10. Palumbo, R.; Ledes, J.; Boutin, O.; Ricart, E. E.; Steinfeld, A.; Moller, S.; Weidenkaff, A.; Fletcher, E. A.; Bielicki, J. *Chem. Eng. Sci.* **1998**, 53, (14), 2503-2517.
11. Shi, J.; Hong, H.; Ding, Y.; Yang, Y.; Wang, F.; Cai, W.; Wang, X. *J. Mater. Chem.* **2011**, 21, (25), 9000-9008.
12. Mokwa, W.; Kohl, D.; Heiland, G. *Surf. Sci.* **1980**, 99, (1), 202-212.
13. Rockett, A. *Springer, New York* **2008**.
14. Tersoff, J.; Vandergon, A. W. D.; Tromp, R. M. *Phys. Rev. Lett.* **1994**, 72, (2), 266-269.
15. Krug, J. *Physica A*. **2002**, 313, (1-2), 47-82.